Knitting algorithm for calculating Green functions in quantum systems

K. Kazymyrenko and X. Waintal
Service de Physique de l'Etat Condensé, DSM/DRECAM/SPEC, CEA Saclay, 91191 Gif Sur Yvette Cedex, France
(Received 19 February 2008; published 17 March 2008)

We propose a fast and versatile algorithm to calculate local and transport properties such as conductance, shot noise, local density of state, and local currents in mesoscopic quantum systems. Within the nonequilibrium Green function formalism, we generalize the recursive Green function technique to tackle multiterminal devices with arbitrary geometries. We apply our method to analyze two recent experiments: an electronic Mach–Zehnder interferometer in a two-dimensional gas and a Hall bar made of graphene nanoribbons in a quantum Hall regime. In the latter case, we find that the Landau edge state pinned to the Dirac point gets diluted upon increasing carrier density.

DOI: 10.1103/PhysRevB.77.115119 PACS number(s): 72.10.Bg, 72.70.+m, 73.23.−b

I. INTRODUCTION

The field of quantum transport at the nanometer scale now includes a large number of systems involving very different physics. Examples include, for instance, mesoscopic devices in two-dimensional heterostructures,[1] graphene nanoribbons,[2] superconducting weak links,[3] molecular electronic devices,[4] and ferromagnetic multilayer nanopillars.[5,6] Although those systems have different structures and geometries, they are all quantum systems connected to the macroscopic world through electrodes, and, consequently, formalisms developed to describe one of them can often be adapted to the others. This is, in particular, the case of the widely used Landauer–Büttiker formalism,[7] which focuses on the scattering properties of the system. The formalism is very intuitive and general. However, it is not well suited when one is interested in what happens *inside* the sample or for performing a microscopic calculation for a given device. An alternative mathematically equivalent approach is referred to as the nonequilibrium Green function (NEGF) formalism.[8,9] NEGF, which is derived from the Keldysh formalism,[10] provides a simple route to compute the physical observables from a microscopic model. It is now an extremely popular numerical approach to a very wide class of physical problems (see references in Ref. 11). For instance, all the references mentioned in the examples above correspond to calculation done with this technique either from *ab initio* or from phenomenological models.[1–6,12,13] At the core of NEGF is the calculation of the retarded Green function G of the mesoscopic region in the presence of the (semi-infinite) electrodes. A straightforward method consists of a direct inversion of the Hamiltonian H. However, when doing so, one is restricted to rather small systems of a few thousand sites: For a system of size L in dimension d, the computing time scales as L^{3d} while the needed memory scales as L^{2d}. An alternative algorithm, known as the recursive Green function technique,[1,5,14] takes advantage of the structure of H to reduce drastically the computing time down to L^{3d-2}, putting systems of a few 10^6 sites within reach. In its original version,[14–16] only the transport properties of the device could be computed, but recent progresses made it possible to get access to observables inside the sample (such as local electronic density or local currents[1,17]) at a cost of L^{2d-1} in memory. The recursive Green function technique suffers, however, from a serious limitation: In its original formulation, it is intrinsically one dimensional, and most applications are done for quasi-one-dimensional bars connected to two electrodes. On the other hand, real devices often have more than two electrodes and more complicated geometries. This paper is devoted to a general versatile algorithm to simulate multiterminal systems with arbitrary geometries and topologies. Earlier works in this direction are scarce. Baranger *et al.*[18] considered the Hall effect in a two-dimensional (2D) cross (a specific code was developed to handle this geometry). Modular algorithms[19,20] allow us to compute the properties of 2D quantum ballistic billiards. Most references with multiterminals involve direct inversions with small system sizes; others involve adaptation of the algorithm to the specific problem at hand.[21,22] Competitors of the present algorithm are also being developed[23,24] by using alternative techniques such as decimation.[25]

In this paper, we show that the recursive Green function algorithm can be generalized to deal with arbitrary geometry, topology, number of connected electrodes, and inner degrees of freedom (like spin for ferromagnets or electron/hole in superconductors). Our algorithm is conceptually simpler than the original, as it is not based on a specific geometry. The sites are added one by one in a manner reminiscent of the knitting of a sweater. The algorithm is optimum in term of speed and a significant gain in memory is also achieved. The method allowed us to study the electronic Mach–Zehnder interferometer[26,27] and anomalous quantum Hall effect in a graphene Hall bar,[28] which have been the subject of recent experiments. Going from the first system to the second required virtually no additional development.

II. NONEQUILIBRIUM GREEN FUNCTION FORMALISM IN A NUTSHELL

We consider a quantum system of N sites connected to several conducting electrodes. We use a general tight-binding Hamiltonian for the system,

$$\hat{H} = \sum_{i \neq j}^{N} t_{ij} c_i^{\dagger} c_j + \sum_{i=1}^{N} \epsilon_i c_i^{\dagger} c_i, \tag{1}$$

where $c_i^{\dagger}$ (c_i) denotes the usual creation (annihilation) operator of an electron on site i. The site index i stands for the

position in space but can also include other possible degrees of freedom like spin or electron/hole. t_{ij} is usually very sparse as only nearest (or next nearest) neighboring sites are connected. The electrodes l are semi-infinite systems at equilibrium with temperature T_l and chemical potential μ_l. They can be "integrated" out of the equations of motion and only appear in the formalism through self-energies Σ_l that provide boundary conditions at the connected sites. We use an algorithm introduced by Ando[29] (see also Ref. 13) for the calculation of those self-energies. The physical observables can be simply related to the nonequilibrium lesser Green function $G^<_{ij}(E)=i\int dt e^{-iEt}\langle c^\dagger_j c_i(t)\rangle$. For instance, the local density ρ_i and current I_{ij} reads

$$\rho_i = \frac{1}{2\pi}\,\mathrm{Im}\int_{-\infty}^{\infty} dE G^<_{ii}(E), \tag{2}$$

$$I_{ij} = \int_{-\infty}^{\infty} dE[t_{ij}G^<_{ji}(E) - t_{ji}G^<_{ij}(E)]. \tag{3}$$

The simplicity of NEGF comes from the fact that in the absence of electronic correlation, $G^<$ (which describes the system out of equilibrium) has a very simple expression in terms of the retarded Green function G: $G^<=G\Sigma^<G^\dagger$, where $\Sigma^<=\Sigma_l f_l(\Sigma_l^\dagger-\Sigma_l)$ and $f_l=1/(1+\exp[(E-\mu_l)/kT_l])$ is the Fermi function. G itself is simply defined in terms of the one-body Hamiltonian matrix $H_{ij}=t_{ij}+\epsilon_i\delta_{ij}$ by

$$G(E) = \frac{1}{E - H - \sum_l \Sigma_l}. \tag{4}$$

III. KNITTING, SEWING, AND UNKNITTING ALGORITHMS

A. Basic idea behind recursive algorithms

The problem of computing $G(E)$ is thus reduced to a conceptually simple task, finding the inverse of the H matrix (to which we implicitly include the self-energies). Our basic tool is to judiciously divide $H=H_0+V$ between an unperturbed part H_0 and a perturbation V. Typically, the perturbation will be the hopping elements that allow us to glue two separated parts of the system together. The Dyson equation $G=g+gVG$, which relates G to the known $g=1/(E-H_0)$, is the corner stone of all recursive algorithms. Suppose that (i) one is interested only in $G_{\alpha\beta}$ for a small subset of sites labeled by α and β (the electrode sites, for instance) and (ii) V_{ij} only connects a small number of sites labeled by i and j. The following glueing sequence allows one to get the needed matrix elements in three steps. The Dyson equation restricted to the connected sites (via V_{ij}) is a *close* equation,

$$G_{ij} = g_{ij} + \sum_{kl} g_{ik}V_{kl}G_{lj}. \tag{5}$$

Since the number of those connected sites is small, the G_{ij} can hence be easily computed. In a second step, one obtains the elements

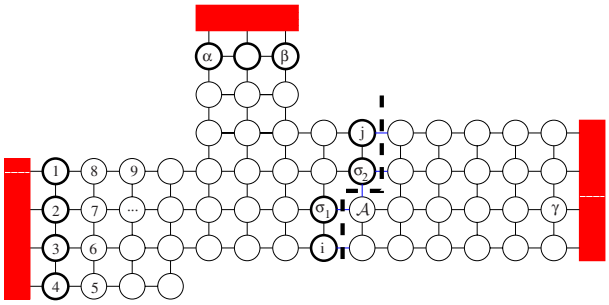

FIG. 1. (Color online) The system scheme and notations. The sites are labeled according to the order in which they are added to the system. The boxes define the three electrodes coupled to the mesoscopic system. The various letters stand for the added site ($\mathcal{A}$), electrode sites (α, β, and γ), connected sites (σ_1 and σ_2), and interface sites (i and j), as discussed in the text. Bold circles indicate sites whose GF elements are updated at the current knitting step. The thick dashed line separates the part already included (left) from the part that is still to be knitted to the system (right).

$$G_{\alpha j} = g_{\alpha j} + \sum_{kl} g_{\alpha k}V_{kl}G_{lj}. \tag{6}$$

In the third step,

$$G_{\alpha\beta} = g_{\alpha\beta} + \sum_{kl} g_{\alpha k}V_{kl}G_{l\beta} \tag{7}$$

are computed. In the original recursive Green function algorithm,[14] the above sequence is used in the following way: One considers a bar of width M and length L. The bar is sliced in L stacks and the perturbation V_{ij} are the hopping elements that connect the different stacks. The system is then built recursively as the stacks are added one at a time, and at each step the glueing sequence is used. The g_{ij} are known either from the previous calculation (for the bar side) or from a numerical direct calculation for the added stack.

B. Knitting algorithm for global transport properties

Our knitting algorithm is based on the same glueing sequence, but the sites are added one by one. We start by indexing the sites according to the order in which they are going to be added to the system. Figure 1 shows a cartoon of a typical system together with the notations used in the following. The main difficulty of the algorithm lies in the bookkeeping of the various Green function elements, and precise definitions are compulsory. At a given stage of the knitting, when we have already included sites $1,\ldots,\mathcal{A}-1$ and are about to include site $\mathcal{A}$, we distinguish between four categories of sites labeled by different indices.

(1) The *connected sites* are the sites that are directly connected to $\mathcal{A}$ via hopping elements $t_{\mathcal{A}\sigma}$. They are labeled by the index σ and appear in a very small number (less than the number of neighbors of a given site $\mathcal{A}$).

(2) The *interface sites* labeled by i and j are the sites that still miss some of their neighbors, i.e., that will be themselves connected sites later in the knitting. Hence, the Green function elements for those sites is to be kept in memory. Note that it is a dynamical definition; i.e., at each step, some

sites appear and others disappear from the interface. The total number M of interface sites scales as a surface $M \propto N^{d-1}$.

(3) The *updated sites* are the sites whose Green function elements are updated at each step of knitting. They belong either to the interface or to the electrodes. They are noted by α and β, bold circles in Fig. 1.

With these notations, we can apply the glueing sequence and express the Green function with the added site $G^{[\mathcal{A}]}$ in terms of the Green function $G^{[\mathcal{A}-1]}$ of the system composed of $\mathcal{A}-1$ sites. The first step reads

$$G^{[\mathcal{A}]}_{\mathcal{A}\mathcal{A}} = 1/\left(E - \epsilon_{\mathcal{A}} - \sum_{\sigma\tilde{\sigma}} t_{\mathcal{A}\sigma} G^{[\mathcal{A}-1]}_{\sigma\tilde{\sigma}} t_{\tilde{\sigma}\mathcal{A}}\right). \tag{8}$$

Note that it is the only place where we actually perform an inversion, and it is done on a scalar quantity. The second step reads

$$G^{[\mathcal{A}]}_{\alpha\mathcal{A}} = \sum_{\sigma} G^{[\mathcal{A}-1]}_{\alpha\sigma} t_{\sigma\mathcal{A}} G^{[\mathcal{A}]}_{\mathcal{A}\mathcal{A}}, \tag{9}$$

$$G^{[\mathcal{A}]}_{\mathcal{A}\beta} = \sum_{\sigma} G^{[\mathcal{A}]}_{\mathcal{A}\mathcal{A}} t_{\mathcal{A}\sigma} G^{[\mathcal{A}-1]}_{\sigma\beta}. \tag{10}$$

The last step concentrates almost all the computing time ($\propto M^2$),

$$G^{[\mathcal{A}]}_{\alpha\beta} = G^{[\mathcal{A}-1]}_{\alpha\beta} + G^{[\mathcal{A}]}_{\alpha\mathcal{A}} \frac{1}{G^{[\mathcal{A}]}_{\mathcal{A}\mathcal{A}}} G^{[\mathcal{A}]}_{\mathcal{A}\beta}. \tag{11}$$

Note that the previous formula has a very simple physical interpretation in terms of paths: The amplitude for an electron to go from site β to site α is the amplitude that avoids site $\mathcal{A}$ plus the amplitude that goes through site $\mathcal{A}$. The factor $1/G^{[\mathcal{A}]}$ removes the double counting of the loops from $\mathcal{A}$ to itself. Once the glueing sequence is completed, the interface is updated: The new site is added while sites that now have all their neighbors can be removed. For instance, in Fig. 1, once site $\mathcal{A}$ has been added, site σ_1 can be deleted from the interface. The previous sequence is iterated until all the N sites have been added to the system. Eventually, we get $G_{\alpha\beta}$ of the entire system. However, we only get the matrix elements between the (few) sites α and β connected to the electrodes. Those matrix elements give access to all transport properties such as conductance and shot noise but no information on what happens inside the sample. The computing time (needed memory) of the knitting algorithm scales as M^2N (M^2), in agreement with the original recursive algorithm for a wire.

C. Sewing algorithm for calculating local observables

We now proceed with extending the knitting algorithm to the calculations of local observables. In practice, we need matrix elements of the type $G_{\alpha r}$ between electrodes and any inner site of the system r. Such an extension has been done in Ref. 1 for the original recursive algorithm: One performs a first recursive calculation and saves the partial Green functions $G^{[r]}_{\alpha r}$ for future use. When the calculation is completed, one starts a new recursive calculation, beginning from *the other* hand of the system. Along the way, one recovers the saved Green functions for the left part of the system and uses the glueing sequence to glue them with the (freshly calculated) Green function of the right part of the system. This scheme can be generalized to an arbitrary geometry as well: We first perform a full knitting calculation. Then, we start backward the sewing algorithm and sew the sites $\mathcal{A}$ one by one in reversed order (i.e., from N to 1). We label sites with an index smaller than $\mathcal{A}$ ("left" part of the system) by indices without a prime $(i,j,\ldots)$ and the sites (strictly) higher than $\mathcal{A}$ ("right") by primed indices $(i',j',\ldots)$. Introducing the "interface self-energy" $\mathbb{S}_{ij} = \Sigma_{i'j'} t_{ij'} G_{j'i'} t_{i'j}$, the glueing sequence reads

$$G_{\alpha\mathcal{A}} = G^{[\mathcal{A}]}_{\alpha\mathcal{A}} + \sum_{ij} G^{[\mathcal{A}]}_{\alpha i} \mathbb{S}_{ij} G^{[\mathcal{A}]}_{j\mathcal{A}}, \tag{12}$$

$$G_{\alpha'\mathcal{A}} = \sum_{j'i} G_{\alpha' j'} t_{j'i} G^{[\mathcal{A}]}_{i\mathcal{A}}. \tag{13}$$

The result of the calculation is then used to update $\mathbb{S}_{ij}$, and one can proceed with $\mathcal{A}-1$, and so on. The drawback of this algorithm is that many ($\sim NM$) matrix elements $G^{[r]}_{\alpha r}$ must be stored during the first knitting calculation, which limit practical calculations to a few hundred thousand sites.

D. Saving memory with unknitting

The last piece of algorithm, called unknitting, allows us to recalculate the matrix elements $G^{[\mathcal{A}]}_{\alpha\mathcal{A}}$ in the backward calculation instead of saving them. Indeed, using the Dyson equation for $H_0 = H - V$, it is possible to "remove" sites from the system and express $G^{[\mathcal{A}-1]}$ as a function of $G^{[\mathcal{A}]}$

$$G^{[\mathcal{A}-1]}_{\alpha\beta} = G^{[\mathcal{A}]}_{\alpha\beta} - G^{[\mathcal{A}]}_{\alpha\mathcal{A}} \frac{1}{G^{[\mathcal{A}]}_{\mathcal{A}\mathcal{A}}} G^{[\mathcal{A}]}_{\mathcal{A}\beta}. \tag{14}$$

The above equation should, however, be taken with care. Indeed the interface is not the same for $G^{[\mathcal{A}-1]}$ and $G^{[\mathcal{A}]}$ so that some of the matrix elements $G^{[\mathcal{A}]}_{\alpha\mathcal{A}}$ on the right hand side are not stored in memory. In the bulk of the system, the interface is of constant size so that there is only one site $\mathcal{R}$ that belongs to the interface of $G^{[\mathcal{A}-1]}$ but not of $G^{[\mathcal{A}]}$. The matrix elements for this site can also be recomputed,

$$G^{[\mathcal{A}-1]}_{\alpha\mathcal{R}} = G^{[\mathcal{A}]}_{\alpha\mathcal{A}} (t_{\mathcal{R}\mathcal{A}} G_{\mathcal{A}\mathcal{A}})^{-1} - \sum_{\sigma\neq\mathcal{R}} G^{[\mathcal{A}-1]}_{\alpha\sigma} t_{\sigma\mathcal{A}} t^{-1}_{\mathcal{R}\mathcal{A}},$$

$$G^{[\mathcal{A}-1]}_{\mathcal{R}\alpha} = (G^{[\mathcal{A}]}_{\mathcal{A}\mathcal{A}} t_{\mathcal{A}\mathcal{R}})^{-1} G^{[\mathcal{A}]}_{\mathcal{A}\alpha} - \sum_{\sigma\neq\mathcal{R}} t^{-1}_{\mathcal{A}\mathcal{R}} t_{\mathcal{A}\sigma} G^{[\mathcal{A}-1]}_{\sigma\alpha},$$

which completes the algorithm. Theoretically, the unknitting algorithm allows us to decrease the memory from MN to $\max(N, M^2)$, hence completely removing the memory bottleneck in the calculations. We found that it is indeed the case in the middle of the tight-binding band where all the channels are conducting. Outside this region, the last equation above is, however, numerically unstable and introduces an error in the calculation that increases as $\exp(aN/M)$. The origin of this instability can be understood from the example

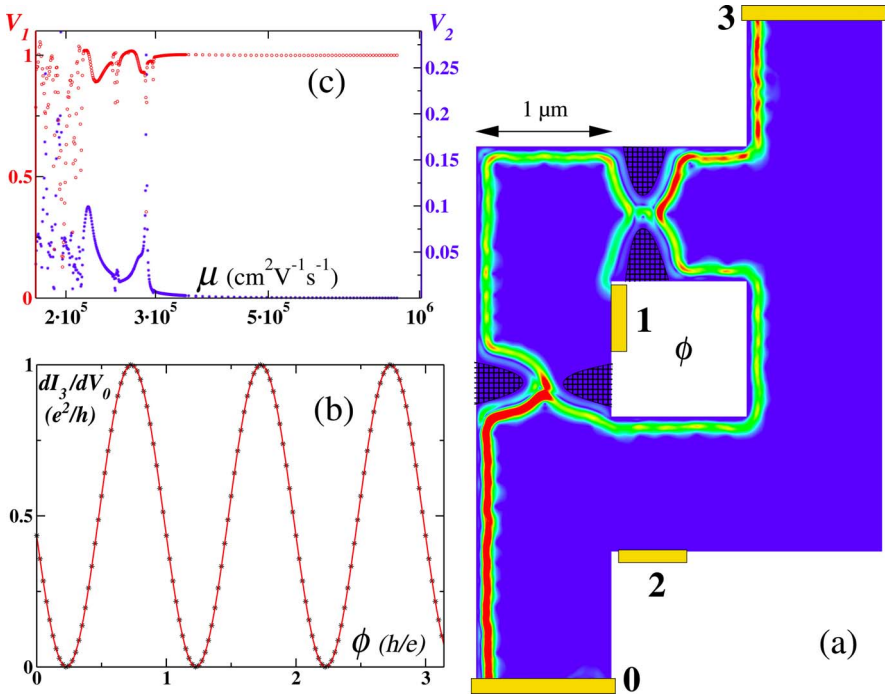

FIG. 2. (Color online) Mach–Zehnder interferometer in a 2D gas modeled by a scalar tight-binding model. The mobility is $\mu = 5 \times 10^5$ cm^2/V s, the electron density is $n_s = 10^{10}$ cm^{-2}, and the magnetic field is $B = 0.2$ T. (a) Local current intensity when a bias voltage is applied to lead 0 and the other contacts are grounded (1.2×10^6 sites; blue corresponds to no current and red to maximum current). (b) Differential conductance dI_3/dV_0 as a function of the number of flux quanta ϕ through the hole. (c) Visibility coefficients $\mathcal{V}_1$ and $\mathcal{V}_2$ (see text) as a function of the electron mobility μ.

of a simple perfect one-dimensional chain with unit hopping. In this case, Eq. (8) takes a simple form, $G^{[\mathcal{A}]} = 1/(E - G^{[\mathcal{A}-1]})$. When $|E| > 2$, the chain is no longer propagative (only evanescent waves can be found), and this equation converges toward a simple attractive fixed point. After several iterations, the convergence is achieved up to numerical precision and the initial condition is lost: The equation can no longer be inverted to follow our steps back. We found that the unknitting algorithm is nevertheless useful. Depending on the precision needed, the matrix elements $G^{[\mathcal{A}]}_{\alpha\mathcal{A}}$ can be saved in the forward calculation only every few sites instead of every site. In practice, in the worst case (bottom of the band where almost all modes are evanescent), we found that a factor of 10 in memory could be gained while keeping the numerical precision better than 10^{-10}.

IV. APPLICATION: MACH–ZEHNDER INTERFEROMETER IN A TWO-DIMENSIONAL ELECTRON GAS

As a first application of our algorithm, we consider a Mach–Zehnder interferometer similar to the ones studied in recent experiments.[27] The devices are made in a two-dimensional high mobility GaAs/AlGaAs heterostructures, which we characterize by its mobility μ, electronic density n_s, size $\mathcal{L}$, and perpendicular magnetic field B. The simulations are performed by discretizing the Schrödinger equation on a square grid with a lattice spacing b. The resulting tight-binding model has nearest neighbor hoppings t and disordered onsite potential, which are chosen randomly within $[-W/2, +W/2]$. The magnetic field is added within a discretized Landau gauge by adding a phase Φ in the hopping elements $t^y_{(n_x,n_y)}$ along the y direction: $t^y_{(n_x,n_y)} = te^{i2\pi\Phi n_x}$ [where (n_x, n_y) is the position on the grid along x and y]. The energy E is measured from the bottom of the band, and we found no significant deviations from the continuum limit as long as we kept $E < 0.1t$. The tight-binding parameters are related to the experimental ones as follows: $n_s = E/(2\pi tb^2)$, $B = \Phi h/(eb^2)$, and $\mu = (e/h)96\pi b^2(t/W)^2$. The latter formula was obtained from a calculation of the Drude conductance of our tight-binding model and was checked by direct numerical calculations. The total number $\mathcal{N} = \mathcal{L}^2 n_s$ of electrons in the sample and the conductance per square $g = e\mu n_s$ are both independent of the discretized step b. The middle of the nth plateau of the quantum Hall effect is found for $n = E/(4\pi t\Phi)$.

The Mach–Zehnder interferometer is the electronic analog of the well-known optical device. The system consists of a loop connected to four contacts, one of which lies in the center part of the loop [see Fig. 2(a)]. The physics involved is fairly straightforward: The system is placed under a high magnetic field in the quantum Hall regime at the first Hall plateau (the current is supported by one edge state). All contacts are grounded except contact 0, which is placed at a slightly higher voltage V_0. The injected current follows the edge channel until it reaches a first quantum point contact (QPC) which works as a perfect beam splitter and is split into two parts [see Fig. 2(a)]. The two edge states are eventually recombined at the second QPC and the current I_3 is collected in contact 3. Along the way, the two edge states pick up a difference of phases that includes the magnetic flux ϕ through the hole. Note that Fig. 2(a) is not a cartoon but an actual calculation of the local density of current injected from lead 0. Along the way, the two edge channels pick up a phase difference that produces interferences. Figure 2(b) shows the differential conductance dI_3/dV_0 in units of e^2/h as a function of flux ϕ (in units of h/e) along with a (almost perfect) sinusoidal fit. Our data are in complete agreement with what is obtained from the Landauer–Büttiker theory. In particular, the visibility $\mathcal{V}_1$ decreases when the transmission

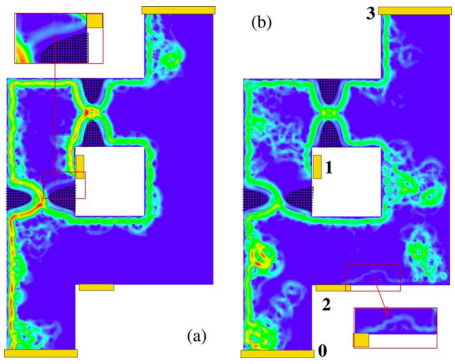

FIG. 3. (Color online) Same as Fig. 2(a) for two dirtier samples with mobility $\mu=3\times10^5$ cm^2/V s (a) and $\mu=2.5\times10^5$ cm^2/V s (b), electron density $n_s=10^{10}$ cm^{-2}, and magnetic field $B=0.2$ T. Zoom of (a) shows the current that escapes the first contact and makes the second loop. It is responsible for the presence of a second visibility harmonic $\mathcal{V}_1=1$ $\mathcal{V}_2=0.1$. Similar zoom of (b) shows backscattered current, which is recovered by contact 2. $\mathcal{V}_1=0.99$ and $\mathcal{V}_2=0.01$.

T of one QPC departs from $1/2$ as $\mathcal{V}_1=2\sqrt{T(1-T)}$.

To proceed further, we increase the disorder in our sample and measure the visibility of the interference pattern as a function of the mobility μ. We find that $dI_3/dV_0(\phi)$ is well fitted by including two harmonics,

$$dI_3/dV_0 \propto 1 + \mathcal{V}_1 \cos 2\pi\phi + \mathcal{V}_2 \cos 4\pi\phi. \quad (15)$$

The parameters $\mathcal{V}_1$ and $\mathcal{V}_2$ are shown in Fig. 2(c) for a typical sample. For $\mu \geq 4\times10^5$ cm^2 V^{-1} s^{-1}, there is no backscattering in the sample and the interference pattern is perfect ($\mathcal{V}_1=1$ and $\mathcal{V}_2=0$). Below 4×10^5 cm^2 V^{-1} s^{-1}, however, backscattering sets in and visibility decreases strongly. More importantly, visibility becomes extremely sensitive to the disorder configuration, and huge sample to sample fluctuations are observed. Simultaneously, the second harmonic $\mathcal{V}_2$ sets in. Those results are readily understood by looking at the current intensities injected from lead 0, as shown in Fig. 3 for two different samples with mobilities slightly lower than that in Fig. 2(a). When the disorder is strong enough, the edge channels get significantly disturbed and are able to reach (partially) the opposite wall [as seen in Fig. 3(b)]. This backscattering leads to a decrease of the visibility. At the same time, a path that avoids contact 1 appears, which causes $\mathcal{V}_2$ to increase [the corresponding path makes a complete tour of the central island, see the inset of Fig. 3(a)]. It is notable that no second harmonic $\mathcal{V}_2$ was observed experimentally, which is, as the samples had a mobility of the order of 10^6 cm^2 V^{-1} s^{-1} or higher,[26,27] consistent with our findings. We conclude that static disorder (or, more trivially, a bad central Ohmic contact) cannot be at the origin of the reduced visibility in these experiments.

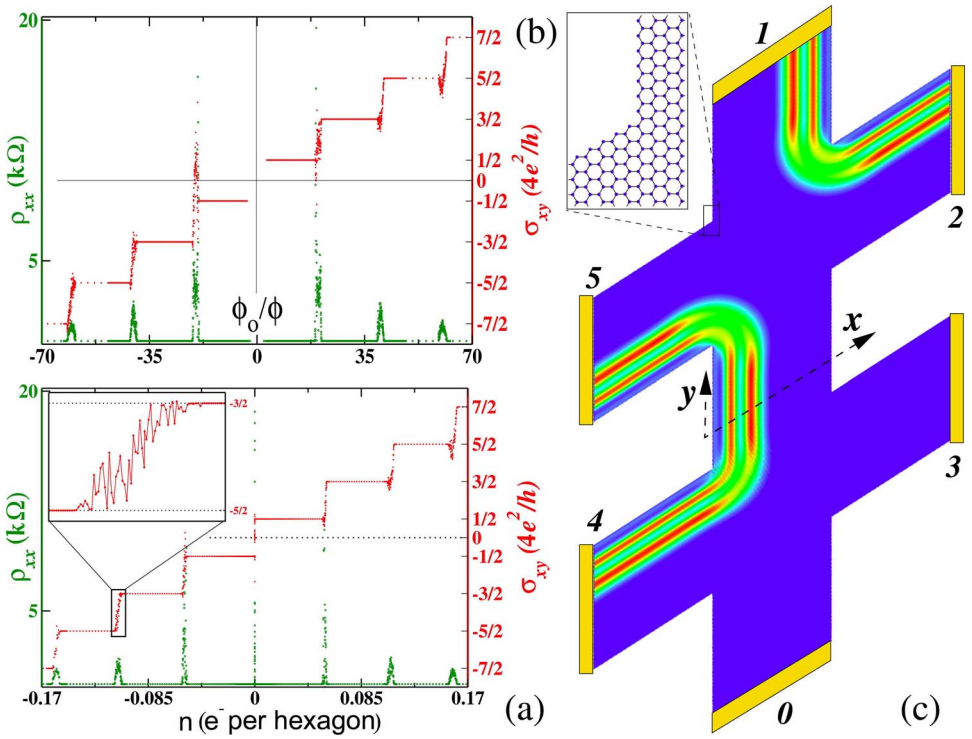

FIG. 4. (Color online) Quantum Hall effect in graphene. Hall conductance σ_{xy} and longitudinal resistance ρ_{xx} are plotted as a function of inverse magnetic field $1/\Phi$ (a) and carrier density n (b) in the presence of a small disordered potential (10% of the hopping matrix elements). In (a) the carrier density is $0.18e$/hexagon, while in (b) a magnetic flux $\Phi=0.014h/e$ per hexagon is applied. The inset of (b) shows a zoom of the transition between plateaus. (c) shows the local current intensity when current is injected from both contacts 1 and 4 (3×10^5 hexagons, $N=2$).

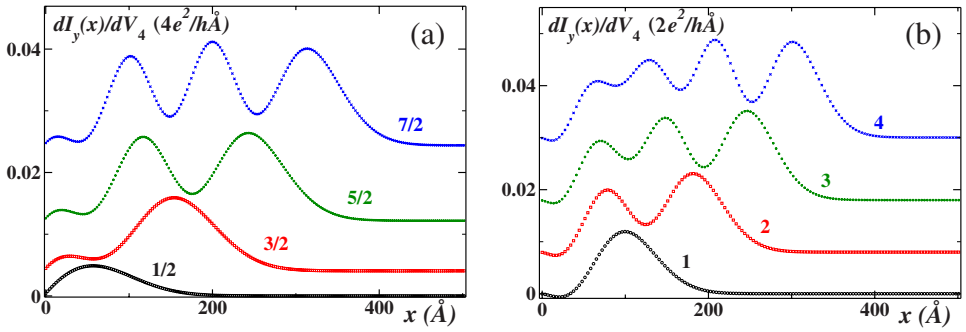

FIG. 5. (Color online) Comparison of the edge channels for a graphene (a) and a semiconductor heterostructure (b) two-dimensional electron gases. The plots show the local current density in the y direction $dI_y(x)/dV$ as a function of the distance x from the border of the sample for four consecutive Hall plateaus corresponding to $N=0,1,2,3$ for graphene (a) and $n=1,2,3,4$ for the heterostructure (b). All graphs are translated for clarity from bottom to top. The magnetic field is $B=14$ T.

V. APPLICATION: ANOMALOUS QUANTUM HALL EFFECT IN A GRAPHENE HALL BAR

In this second application, we consider a Hall bar in graphene in the quantum Hall regime [see Fig. 4(c)]. We used the standard tight-binding approach[30] for the graphene hexagonal lattice, where each site represents a carbon atom and is connected to his neighbors by a hopping t. We use zigzag edges for the system and the leads that are semi-infinite nanoribbons. To avoid reflection at the lead/system interface, the leads also include the magnetic field. The magnetic field is included within a gauge similar to the one used for the Mach–Zehnder above by introducing a phase Φ in the hopping elements between the A and B sites. Noting a (1.42 Å), the distance between carbon atoms, the electronic density n_s and magnetic field B are related to E/t and the total flux Φ (in unit of h/e) per hexagon as follows: $n_s=(E/at)^2 4/(9\pi)$ and $B=2h\Phi/(3\sqrt{3}ea^2)$. The middle of Nth Hall plateau is found for $N+1/2=E^2/(2\sqrt{3}\pi\Phi t^2)$.

Figure 4 shows the transverse conductance and longitudinal resistance as a function of carrier density (a) or inverse magnetic flux (b) for a graphene Hall bar. Our results for a mesoscopic Hall bar are numerical counterparts to the experimental data of Ref. 28. In particular, we recover the presence of plateaus in the transverse conductance at quantized values $(N+1/2)4e^2/h$. The $N=0$ plateau corresponds to a Landau level pinned to the Dirac point and is special to the Dirac equation symmetry class. We also observe mesoscopic fluctuations at the transition between plateaus similar to those known in usual 2D gases [see the inset of Fig. 4(a)]. The edge current density at $N=2$ injected simultaneously from contacts 1 and 4 is plotted in Fig. 4(c), which is the graphene counterpart to Fig. 2(c).

We note one important difference between the edge states of graphene and those of a regular heterostructure: While Fig. 4(c) has been made for $N=2$, i.e., for the third plateau in the sequence, one observes only two peaks in the local current density, i.e., apparently two edge states only. This is revealed more quantitatively in Fig. 5 where we have plotted the cross section of the current density for the first plateaus of both the graphene $(N=0,1,2,3)$ and the heterostructure $(n=1,2,3,4)$. The areas under those curves correspond, respectively, to 1/2, 3/2, 5/2, and 7/2 in the graphene and to 1, 2, 3, and 4 in the heterostructure. The numbers of peaks, however, is 1, 1, 2, and 3 and 1, 2, 3, and 4, respectively, so that the $N=0$ peak (corresponding to the $E=0$ Landau level) gets blurred behind the other peaks upon increasing carrier density. This peculiar behavior could possibly be observed in scanning tunneling microscopy or local compressibility experiments.[31]

VI. CONCLUSION

We have presented a set of algorithms that allows us to calculate the transport and local properties of a generic class of tight-binding models. Using the unknitting technique, some significant gain of memory could be gained with respect to previous techniques. However, our main point here is the global simplicity of the algorithm. We could easily implement it to get a versatile code that treats complicated geometries, such as the ones presented in the applications, with the same ease as one treats the usual quasi-one-dimensional bar, ubiquitous in the literature.

ACKNOWLEDGMENTS

We wish to thank O. Parcollet, A. Freyn, and F. Portier for useful discussions. Financial support from region "Ile de France" as well as from EC Contract No. IST-033749 "DynaMax" is acknowledged.

APPENDIX: IMPLEMENTATION TIPS

In this appendix, we have grouped a few technical points that can help us to get significant gains in computing time or, maybe more importantly, in human development time.

(1) The computing time for adding one site in the knitting algorithm is dominated by the last step of the glueing sequence [Eq. (11)] and scales as $O(M^2)$. Hence, almost all the computing time of the algorithm is concentrated in a single line of code, which can be optimized aggressively. The best results were obtained by using low level BLAS routines for this simple step. Note that the only inversions that take place in the algorithm are scalars: At no point do we need to rely

on matrix inversion routines in contrast to the original recursive technique.

(2) A practical difficulty is to maintain dynamically the list of active *interface* sites. We use the following simple algorithm: To each *interface* site is associated a list of the site's neighbors that have not yet been knitted to the system. As new sites are knitted to the system, this list is updated. When a site has all his neighbors knitted, he can be removed from the interface.

(3) The algorithms described in this paper allow us to solve a very generic class of tight-binding models. Almost as important as those solvers is the ability to easily construct new systems. In our implementation, we represent internally a system as a generic graph: Each site possesses the list of its neighbors, together with the corresponding matrix elements. A set of routines is used to operate on those graphs. A very important one is a function that allows us to stick two systems together by identifying some sites of the two systems. This routine allows us to construct a system from small pieces in a "legolike" way. For instance, the system of Fig. 2(c) is obtained in four lines of code by "sticking" four rectangular systems together.

(4) The intensive pieces of the code should be written in a low level language (in our case, C++). However, we have found that a very significant gain in developing time could be obtained by making use of the code in a higher level script language. In our case, we use Python, and the automatic wrapping of the C++ code into the Python API has been done with SWIG. The system constructions, calculation and plotting are done in small Python programs that constitute our input files.

[1] G. Metalidis and P. Bruno, Phys. Rev. B **72**, 235304 (2005).
[2] A. Rycerz and C. W. J. Beenakker, arXiv:0709.3397 (unpublished).
[3] U. Gunsenheimer and A. D. Zaikin, Phys. Rev. B **50**, 6317 (1994).
[4] P. S. Damle, A. W. Ghosh, and S. Datta, Phys. Rev. B **64**, 201403(R) (2001).
[5] S. Sanvito, C. J. Lambert, J. H. Jefferson, and A. M. Bratkovsky, Phys. Rev. B **59**, 11936 (1999).
[6] P. M. Haney, D. Waldron, R. A. Duine, A. S. Nunez, H. Guo, and A. H. MacDonald, Phys. Rev. B **76**, 024404 (2007).
[7] Y. M. Blanter and M. Buttiker, Phys. Rep. **336**, 1 (2000).
[8] P. N. C. Caroli, R. Combescot, and D. Saint-James, J. Phys. C **4**, 916 (1971).
[9] Y. Meir and N. S. Wingreen, Phys. Rev. Lett. **68**, 2512 (1992).
[10] L. Keldysh, Zh. Eksp. Teor. Fiz. **47**, 1515 (1964).
[11] R. K. Lake and R. R. Pandey, arXiv:cond-mat/0607219 (unpublished).
[12] M. Brandbyge, J.-L. Mozos, P. Ordejón, J. Taylor, and K. Stokbro, Phys. Rev. B **65**, 165401 (2002).
[13] P. A. Khomyakov, G. Brocks, V. Karpan, M. Zwierzycki, and P. J. Kelly, Phys. Rev. B **72**, 035450 (2005).
[14] A. MacKinnon, Z. Phys. B: Condens. Matter **59**, 385 (1985).
[15] D. J. Thouless and S. Kirkpatrick, J. Phys. C **14**, 235 (1981).
[16] P. A. Lee and D. S. Fisher, Phys. Rev. Lett. **47**, 882 (1981).
[17] A. Cresti, R. Farchioni, G. Grosso, and G. P. Parravicini, Phys. Rev. B **68**, 075306 (2003).
[18] H. U. Baranger, D. P. DiVincenzo, R. A. Jalabert, and A. D. Stone, Phys. Rev. B **44**, 10637 (1991).
[19] S. Rotter, B. Weingartner, N. Rohringer, and J. Burgdörfer, Phys. Rev. B **68**, 165302 (2003).
[20] F. Sols, M. Macucci, U. Ravaioli, and K. Hess, J. Appl. Phys. **66**, 3892 (1989).
[21] P. K. Polinák, C. J. Lambert, J. Koltai, and J. Cserti, Phys. Rev. B **74**, 132508 (2006).
[22] D. Guan, U. Ravaioli, R. W. Giannetta, M. Hannan, I. Adesida, and M. R. Melloch, Phys. Rev. B **67**, 205328 (2003).
[23] J. P. Robinson and H. Schomerus, Phys. Rev. B **76**, 115430 (2007).
[24] M. Wimmer, I. Adagideli, S. Berber, D. Tomanek, and K. Richter, arXiv:0709.3244 (unpublished).
[25] H. M. Pastawski and E. Medina, Rev. Mex. Fis. **47**, 1 (2001).
[26] Y. Ji, Y. Chung, D. Sprinzak, M. Heiblum, D. Mahalu, and H. Shtrikman, Nature (London) **422**, 415 (2003).
[27] P. Roulleau, F. Portier, D. C. Glattli, P. Roche, A. Cavanna, G. Faini, U. Gennser, and D. Mailly, Phys. Rev. B **76**, 161309(R) (2007).
[28] K. S. Novoselov, A. K. Geim, S. V. Morozov, D. Jiang, M. I. Katsnelson, I. V. Grigorieva, S. V. Dubonos, and A. A. Firsov, Nature (London) **438**, 197 (2005).
[29] T. Ando, Phys. Rev. B **44**, 8017 (1991).
[30] A. H. C. Neto, F. Guinea, N. M. R. Peres, K. S. Novoselov, and A. K. Geim, Rev. Mod. Phys. (to be published).
[31] N. B. Zhitenev, T. A. Fulton, A. Yacoby, H. F. Hess, L. N. Pfeiffer, and K. West, Nature (London) **404**, 473 (2000).